

Cite this: DOI: 10.1039/xxxxxxxxxx

Signatures of slip in dewetting polymer films[†]

Dirk Peschka,^a Sabrina Haefner,^b Karin Jacobs,^b Andreas Münch,^c Barbara Wagner^aReceived Date
Accepted Date

DOI: 10.1039/xxxxxxxxxx

www.rsc.org/journalname

Thin liquid polymer films on hydrophobic substrates are susceptible to rupture and formation of holes, which in turn initiate a complex dewetting process that ultimately evolves into characteristic stationary droplet patterns. Experimental and theoretical studies suggest that the specific type of droplet pattern largely depends on the nature of the polymer-substrate boundary condition. To follow the morphological evolution numerically over long time scales and to resolve the multiple length scales involved has so far been a major challenge. In this study a highly adaptive finite-element based numerical scheme is presented that allows for large-scale simulations to follow the evolution of the dewetting process deep into the nonlinear regime of the model equations, capturing the complex dynamics including shedding of droplets. In addition, the numerical results predict the previously unknown shedding of satellite droplets during the destabilisation of liquid ridges, that form during the late stages of the dewetting process. While the formation of satellite droplets is well-known in the context of elongating fluid filaments and jets, we show here that for dewetting liquid ridges this property can be dramatically altered by the interfacial condition between polymer and substrate, namely slip. This work shows how in general interface properties can be systematically used to influence pattern formation processes.

1 Introduction

In fluid mechanics, the no-slip condition is widely accepted as the appropriate boundary condition for flows of Newtonian liquids sheared along a solid surface. A notable exception arises in the presence of a moving contact line between a liquid and the solid substrate, where the use of the no-slip condition leads to a singularity in the stress field^{2,3}. In the past decades, however, it has been shown that thin films of polymer melts can exhibit significant slip when sheared along a substrate, where slip lengths much larger than the film thickness have been observed^{4–10}.

For retracting rims, as they emerge after a hole or trench has opened, the magnitude of slip has a direct impact on its shape and dynamics. When slip is very small or zero, the retraction rate is independent of the size of the growing rim and hence approximately constant, except for logarithmic corrections¹¹. For slip that is large compared to the film thickness, viscous dissipation increases with the rim size and this gives rise to a $t^{-1/3}$ power law in time t for the retraction (dewetting) rate¹², and has been confirmed experimentally^{13–16}. In both cases, the moving rim is susceptible to span-wise instabilities^{17–19}, but for the case where slip is large compared to the film thickness, the dependence of the

retraction velocity on the local rim size provides a crucial amplifying mechanism for the instability, which is absent in the no-slip situation²⁰. As a consequence, the repeated shedding of droplets during dewetting leaves a characteristic pattern, that is absent for systems with no-slip. In either case, the dewetting rims eventually meet to form residual ridges, which in either case are susceptible to a Rayleigh-Plateau type instability with almost the same dominant wave-length²¹. Eventually, this leads to the break-up into droplets. As a result of this long-time process, a strikingly different droplet patterns is obtained, as shown in experiments, see Fig. 1.

The evolution of the polymer melts during these dewetting regimes, from early dewetting stages after hole formation to the late stages of rupture of the ridges, where the hole boundaries meet, is most conveniently modelled by thin-film models. A systematic asymptotic derivation from full Navier-Stokes equations^{22,23}, exploiting the separation between the lateral and normal length, revealed that the resulting dimension-reduced thin-film model depends on the order of magnitude of slip, leading to two asymptotic distinguished limits: a weak-slip and a strong-slip regime, with important limits given by the no-slip and intermediate-slip cases.

While thin-film models have been shown to be of great advantage for the analysis of free boundary problems, predicting the evolution over long time and large spatial scales deep into the nonlinear regimes is still an extremely difficult task. A major problem is to resolve the length scales associated with nanoscopic

^a Weierstrass Institute for Applied Analysis and Stochastics, Mohrenstr. 39, 10117 Berlin, Germany. E-mail: dirk.peschka@wias-berlin.de

^b FR 7.2 Experimentalphysik, Saarland University, 66041 Saarbrücken, Germany.

^c Mathematical Institute, University of Oxford, Andrew Wiles Building, Oxford OX2 6GG, UK.

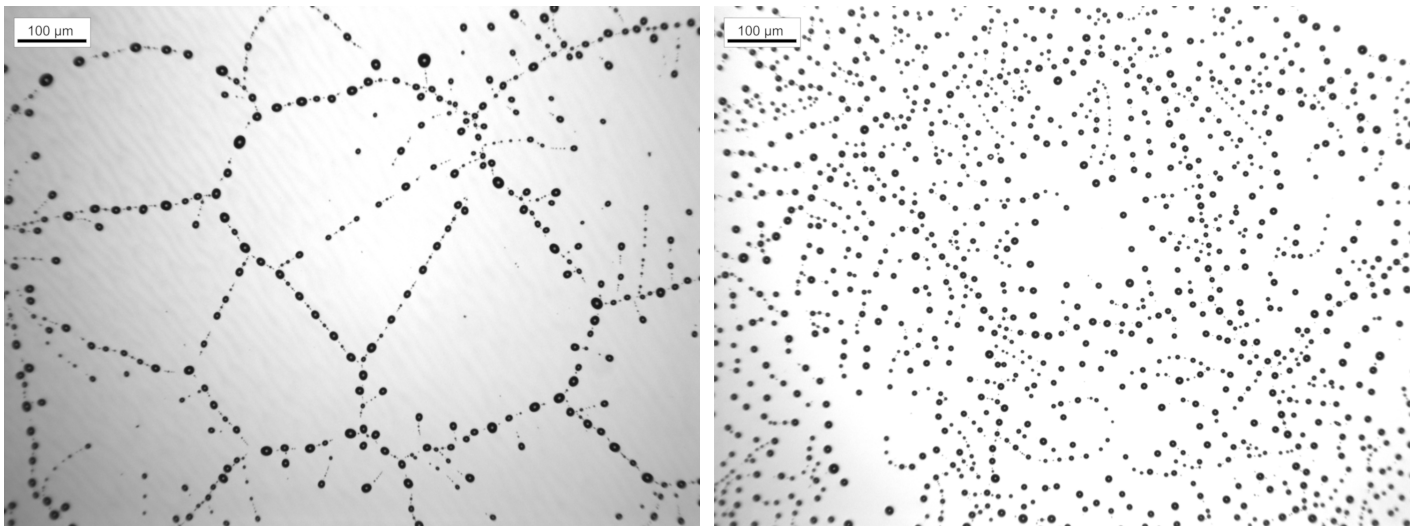


Fig. 1 Stationary droplet pattern of a 110 nm thick polystyrene PS(10.3k) film after dewetting at $T = 120^\circ\text{C}$ from a hydrophobically coated Si wafer: (**left**) AF 1600 and (**right**) DTS coating (Images: Courtesy of L. Marquant¹)

residual layers that remain after the film has dewetted, typically about $\sim 0.1 - 1\text{ nm}$, up to thickness of about $\sim 10 - 1000\text{ nm}$ of the growing rim, and to account for the slip length in the range of $1 - 1000\text{ nm}$, and the length scale of the resulting instability $10^3 - 10^4\text{ nm}$. By far the greatest challenge is to make predictions regarding phenomena on the length scales of the instabilities, while using numerical solutions with a fine spatial resolution on the length scale of the residual layer.

In this article we present a numerical algorithm that is able to answer this need featuring a strategy for local adaptivity and an optimized treatment of the intermolecular potential. We will show that the difference in slip lengths indeed leads to the instability patterns seen in experiments. Our numerical solutions also confirm the Rayleigh-Plateau type instability of the residual ridges during the late phases of the dewetting for both cases, the no-slip and the intermediate-slip cases, with similar wave-lengths at the onset, which had been predicted previously based on a linear stability analysis^{18,21}. Similar studies were concerned with cases of infinite ridges with²⁴ and without²⁵ gravity, followed by a broad range of investigations in the literature for this situation using different contact line models and approximations. Numerically, the work by Diez et al.²⁶ focuses on finite length ridges but also includes a review and elucidating comparison of results for the infinite case. Here, most unstable modes are due to varicose perturbations, and the preferred wave-length of the instability is set by the balance of the destabilising capillary forces, contact-line conditions, and, for sufficiently viscous liquids, by the viscous dissipation. Stability analysis of the effect of slip vs. no-slip on the instability of a stationary ridge show that both are linearly unstable and have similar wave-lengths^{18,21}.

Our numerical methods allow to follow the evolution until rupture and show significant morphological differences. In particular, they reveal that while for the no-slip case the break-up is accompanied by the formation of a cascade of satellite droplets, that has never been seen before in this context. Moreover, for the intermediate-slip case they disappear.

In other contexts such as liquid jets or fluid filaments, satellite droplets during rupture are well-known, see e.g. the work by Tjahjadi et al.²⁷ or the review by Eggers and Villermiaux²⁸. Here, we show for the first time that while the self-repeating rupture of satellite droplets is established for the no-slip boundary condition of a rupturing ridge, they disappear for the intermediate-slip condition. Interestingly, a closer look at experimental results validates these predictions.

In the following sections we first introduce the underlying model equations governing the long-time dewetting process. We revisit analytical results on dewetting rates and their connection to the destabilisation of the rim during the early stages of the dewetting film in section 2. We compare the predictions to experimental results in section 2.3.

To capture the morphological details well-into the nonlinear regime including droplet pin-off scenarios, observed in experiments, we introduce in section 3 a highly adaptive numerical method necessary to bridge the multiple length scales over long time regimes. In section 4 we address the late scenario when the rims of the holes meet and eventually disintegrate into droplets, where we predict a new scenario of cascades of satellite droplets for the no-slip case.

2 Thin-film models and instability

2.1 Problem formulation

Once the film has ruptured by nucleation or by external forcing, forming a hole, or, in a planar-symmetric setting, a trench, the viscous fluid retracts to reduce the overall energy of the liquid-gas, solid-liquid and solid-gas interfaces. The dewetting process is driven by the intermolecular potential ϕ between the film and the substrate, that is given, in the simplest case, by the attractive long-range van-der-Waals forces and short-range Born repulsion forces, the minimum of which yields the height h_* that is left behind after the film has dewetted. Motivated by Lennard-Jones potentials, one often finds intermolecular potentials^{29,30} of the

standard form $\phi(h) = \tilde{\phi}(h/h_*)$, where

$$\tilde{\phi}(h) = \frac{(-S)}{n-m} (nh^{-m} - mh^{-n}), \quad (1)$$

with $m = 2, n = 8$, $\phi'(h_*) = 0$ and $\phi(h_*) = -S$. For partial wetting the spreading coefficient is negative and hence $S < 0$.

Due to the slow dewetting rates of the polymer films with chain lengths below the entanglement lengths, the Navier-Stokes equations serve as the underlying model for the viscous fluid but with an effective slip boundary condition at the substrate. The scale separation of the characteristic length scale H normal and the length scales L tangential to the substrate allow a consistent thin-film approximation in the small parameter $\varepsilon \approx H/L \ll 1$ that leads to the reduction of the free-boundary problem to a problem for the free boundary h in closed form. We assume that the time-dependent domain $\Omega(t) \subset \mathbb{R}^3$ occupied by the viscous fluid can be parametrized using a nonnegative scalar function $h : [0, T] \times \bar{\Omega} \rightarrow [0, \infty)$ such that

$$\Omega(t) = \{(\mathbf{x}, z) : \mathbf{x} \in \bar{\Omega}, 0 < z < h(t, \mathbf{x})\}, \quad (2)$$

where the film height $h(t, \mathbf{x})$ depends on time $t \in [0, T]$ and on space $\mathbf{x} = (x, y) \in \bar{\Omega} \subset \mathbb{R}^2$ with given initial data $h_0(\mathbf{x}) = h(t=0, \mathbf{x})$ (see Fig. 2). It has been shown that depending on the magnitude of (effective) slip length there exist two asymptotic distinguished limits²², leading to the weak-slip thin-film model, given by the fourth-order parabolic partial differential equation (PDE)

$$\partial_t h - \nabla \cdot (m(h) \nabla \pi) = 0. \quad (3a)$$

where the mobility is

$$m(h) = h^3 + bh^2 \quad (3b)$$

and the generalized pressure π is defined as the functional derivative of the energy functional

$$E(h) = \int_{\bar{\Omega}} \frac{1}{2} |\nabla h|^2 + \phi(h) \, d\mathbf{x}, \quad (3c)$$

with respect to h , that is,

$$\pi = \frac{\delta E}{\delta h} = -\nabla^2 h + \Pi(h), \quad (3d)$$

and $\Pi(h) = \partial_h \phi(h)$ is the derivative of the intermolecular potential.

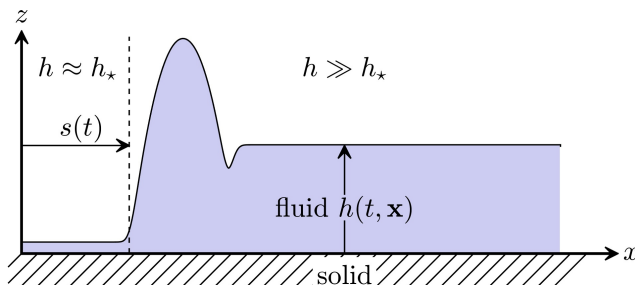


Fig. 2 Sketch of solution $h(t, \mathbf{x})$ in the $x-z$ plane.

The second distinguished limit leads to the strong-slip thin-film

model given by the system of partial differential equations for h and the lateral velocity $\mathbf{u} = (u, v)$ with components u and v in the x and y -direction, respectively

$$\text{Re} (\partial_t \mathbf{u} + (\mathbf{u} \cdot \nabla) \mathbf{u}) = \frac{1}{h} \nabla \cdot \boldsymbol{\sigma} - \nabla \pi - \beta^{-1} \frac{\mathbf{u}}{h} \quad (4a)$$

$$\partial_t h + \nabla \cdot (h \mathbf{u}) = 0, \quad (4b)$$

where Re is the Reynolds number and β is related to the slip length b via $b = \beta/\varepsilon^2$ and the effective shear stress is

$$\boldsymbol{\sigma} = h [\nabla \mathbf{u} + (\nabla \mathbf{u})^\top + 2(\nabla \cdot \mathbf{u}) \mathbb{I}]. \quad (4c)$$

The important limiting cases are the well-known no-slip model, where the degenerate mobility is $m(h) = h^3$ and the so-called intermediate-slip model, that is sometimes also referred to as the full-slip model, with the degenerate mobility $m(h) = h^2$. The details of the dynamic and morphological evolution strongly depend on the magnitude of slip at the solid-liquid interface as has been shown in the literature³¹. For no-slip or weak-slip the liquid accumulates in a growing rim in front of the contact-line, and destabilizes. The case of strong-slip is characterised by very asymmetric retracting rim solutions with a monotone spatial decay towards the unperturbed film for particularly large slip, that undergoes a transition to oscillatory decay for as the slip length decreases below a critical value^{22,32}. This observation has been used to identify the strong slip regime in experiments and in fact also to determine the amount of slip quantitatively^{33–35}, and investigate the molecular causes of slip in polymer melts³⁶. An overview about this topic can be found in the work by Bäumchen and Jacobs³⁷.

2.2 Dewetting rates

We first discuss the dynamics of the cross section of an unperturbed rim, i.e. where $\partial_x h = 0$. In the case of no-slip, $m(h) = h^3$, the evolution is determined by the region near the effective contact line where the rim meets the residual film of thickness of about $h = h_*$ that is left behind the dewetting front. A careful asymptotic analysis and comparison with long-time numerical solutions^{22,38} reveals that the dewetting rate is nearly constant and in fact the position of the contact line $s(t)$ is, to leading order, given by the nearly linear law

$$s(t) \sim \frac{t \tan^3(\theta)}{\ln(3(h_\infty/h_*)t)} \quad (5)$$

as $t \rightarrow \infty$, where $h_\infty = \lim_{x \rightarrow \infty} h$. Physically, this reflects the fact that the size of the rim only has a weak effect on the total friction and hence in turn on the dewetting velocity.

For intermediate slip, where $m(h) = h^2$, the evolution of the unperturbed rim is different. At any given size, the rim behaves like a traveling wave, but with a wave speed that depends on the size of the rim, which by mass conservation is proportional to the distance travelled. A detailed asymptotic analysis^{22,38} that matches the rim to the unperturbed and the residual film gives

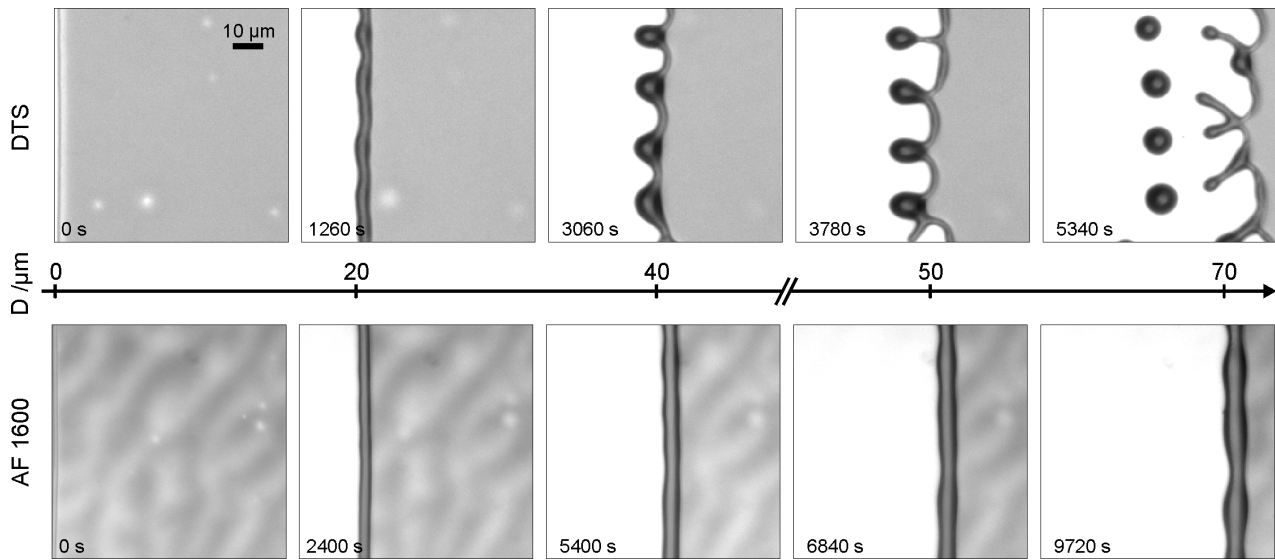


Fig. 3 Series of micrographs characteristic for experiments for films exposed to intermediate (**upper row**, dewetting off hydrophobized Si wafer covered with a silane monolayer DTS) and to no-slip (**lower row**, dewetting off AF 1600-covered Si-wafer). In both series, a 100 nm thin PS(13.7k) film dewets at $T = 120^\circ\text{C}$. In both series, undulations are formed along the rim, however, only in the intermediate slip case above budding is observed that later leads to fingers and a pinch-off of droplets. Comparing rims that have travelled a similar distance ensures that only rims of similar volumes are evaluated.

the leading order result

$$s(t) \sim \left(\frac{9Mb \tan^5 \theta}{4h_\infty} \right)^{1/3} t^{2/3}. \quad (6)$$

in the limit $t \rightarrow \infty$, where b is the slip length and $M \approx 0.0272$. A similar prediction had been made by Reiter and Khanna¹³.

Rims with capillary humps like the ones that appear here are known to be subject to Rayleigh-Plateau like instabilities^{21,24,26}, where the higher capillary pressure in thinner parts squeezes even more liquid into the thicker parts, hence promoting the growth of undulations along the rim. The linear stability of dewetting rims is complicated by the fact that the base state itself grows in time, giving rise to a linearised PDE that cannot be solved exactly using separation of variables. Instead, the linearised PDE can be solved numerically, and the amplification of an initial perturbation tracked in time⁴⁰. Interestingly, the perturbation evolves into a universal long-time shape that is not sensitive to the initial perturbation. Comparing these shapes reveals an important difference between the no-slip and the intermediate slip case: The former is much more symmetric and closer to the classical varicose mode observed in the Rayleigh-Plateau instability than the latter. Moreover, the maximum amplification was significantly higher for the intermediate slip case.

These results were analysed further using an asymptotic sharp-interface approach for large rims and a WKB analysis, which established that the long-time dominant wave-number is given by an equal area rule and is shorter than predicted by a frozen-mode analysis^{41,42}. Direct numerical simulations of the nonlinear PDE with perturbed rims as initial data confirm that indeed, the intermediate slip is much more unstable than the no-slip case, and perturbations grow asymmetrically²¹, as shown in Fig. 8. It is clearly seen that the perturbations in the rim for the no-slip case remain small, while in the intermediate-slip case, they grow, giving

rise to fingers that eventually pinch-off and then the process repeats itself. This is seen also in experimental data in Fig. 3. The physical explanation for these different manifestations relates to the size-dependence of the friction. In the intermediate slip case, thicker parts of a perturbed rim have a smaller velocity than thinner ones and tend to lag further behind. This supplies an additional instability mechanism that reinforces the Rayleigh-Plateau instability, but is essentially absent in the no-slip case where the dewetting rate is largely independent of the rim size^{19,40,42}.

The size dependence also adds another instability mechanism by causing thicker parts of the rim to lag behind thinner parts, thus reinforcing the Rayleigh-Plateau instability and making it more asymmetric¹⁹. A linear stability analysis of the thin-film model predicts the instability to thus be much more pronounced in the intermediate-slip than in the no-slip case^{40–42}.

For slip lengths that are much larger than the film height, the dynamics of the evolution changes yet again. In the strong slip regime, the fluid flow is plug-flow and the evolution is described by a system of PDEs for the film height and for the plug velocity, where the contribution from elongational stresses enters to the same order as the effects from the friction due to slip. Dewetting rim solutions of this model were explored numerically and asymptotically^{22,32}. In this regime, the shape of the profile becomes highly asymmetric, with a steep side facing the dewetted area and a much flatter decay to the unperturbed film. This is well reflected in the experimental data for melts with larger polymer chains, where slip is expected to be larger. Interestingly, the change in the balance of stresses leads to an approximately linear dewetting law,

$$s(t) \sim \frac{b^{1/2} \tan^2(\theta) t}{4\sqrt{2} h_\infty^{1/2} \ln^{1/2} t} \quad (7)$$

that is, another case with an approximately constant velocity of the retracting rim, just as in the no-slip case. This suggests that

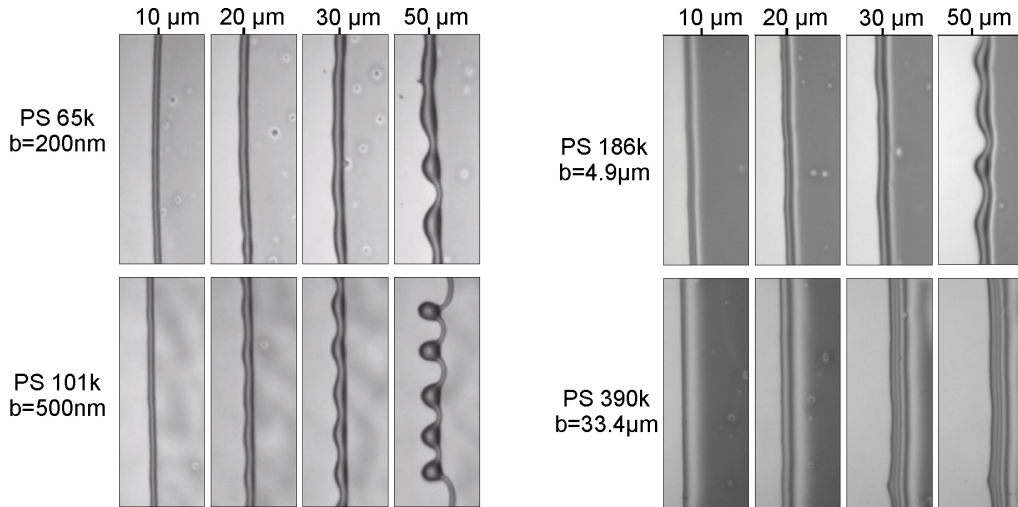


Fig. 4 Comparisons of the dewetting behaviors of 110 nm thick PS films for different chain lengths, dewetting from AF1600 after the rim travelled the distance D given above the images. Films have been annealed to different temperatures to speed up dewetting in case of films with larger viscosities: PS(65k) at $T = 140^\circ\text{C}$, PS(101k) at $T = 140^\circ\text{C}$, PS(186k) at $T = 150^\circ\text{C}$, PS(390k) at $T = 150^\circ\text{C}$. In the chosen systems, the slip length increases with increasing molecular weight, leading to $B = b/h$ of 1.81, 4.6, 45 and 300, respectively. The slip lengths are obtained by fitting the rim profile as reported by Bäumchen et al.³⁶ or McGraw et al.³⁹. Clearly, fingering is suppressed for stronger slip in this system.

for very large slip lengths, the rim should become stable again.

2.3 Experimental set-up and methods

For the experiments, atactic polystyrene (PS, purchased from PSS, Mainz, Germany, molecular weights as listed in the experiments) is used as a model viscous liquid. The films were produced by spin-casting a toluene solution (Selectipur or LiChrosolv, Merck, Darmstadt) of PS on freshly cleaved mica sheets. The glassy thin-films were then floated onto an ultrapure water (organic impurities < 6 ppb, resistance at 25°C : < 18.2 M Ω cm) surface and were then picked up with hydrophobic Si wafers.

Hydrophobic Si wafers were achieved by two different preparation methods: i) on the cleaned Si surface, a self assembled monolayer (SAM) of silane molecules (dodecyltrichlorosilane, DTS, Sigma Aldrich/Merck) was prepared⁴³, or ii) the cleaned Si wafer was dipped into a solution of a fluoropolymer layer (AF1600, Sigma Aldrich/Merck, Darmstadt, Germany).

Dewetting can be initiated by the glassy polymer film above its glass transition temperature. The dewetting of the retracting straight fronts was monitored *in situ* by optical microscopy on a heating plate (Linkam) or by atomic force microscopy (AFM, Dimension ICON, Bruker).

The dewetted distance was typically obtained from optical micrographs. In AFM experiments, the dewetted distance can also be calculated from three-dimensional scans of the rim on the basis of volume preservation. The values resulting from both approaches were checked for consistency.

Slip lengths have been calculated using the rim profile analysis method^{44,45}; structural details, surface roughness values, and wetting properties of the coatings are given in the Supplementary Material to Ref.³¹. Polymer film thicknesses have been determined by ellipsometry on the glassy film or by AFM on the edge of a film.

The experimental results show in Fig. 4 support the prediction of the linear law (7), that for the strong-slip case the instability is suppressed, see the results for the largest slip length in the lower right figure for PS 390k in Fig. 4.

3 Numerical methods

3.1 Finite element solution

We now explain the intricacies of numerically resolving the multiple length scales of the problem. We focus on the two cases of no-slip and intermediate-slip as most of the experimental results regarding the various instabilities fall into either of these two regimes.

Our solution of the thin-film model (3) is based on a P_2 finite element method (FEM), where the fourth-order equation is split into a system of two second-order equations. The FEM uses piecewise quadratic elements and local mesh refinement. We employ a semi-implicit time-discretization, where only the highest order derivative is treated implicitly. Therefore, the thin-film equation (3) is multiplied with a test-function v and integrated by parts and to obtain

$$\int_{\bar{\Omega}} \partial_t h v + m(h) \nabla \pi \cdot \nabla v \, d\mathbf{x} = 0, \quad (8a)$$

where boundary terms vanish due to the no-flux boundary condition $\mathbf{n} \cdot \nabla \pi = 0$ imposed on $\partial \bar{\Omega}$. We also rewrite the pressure π in the weak form as

$$\int_{\bar{\Omega}} \pi v \, d\mathbf{x} = \int_{\bar{\Omega}} \nabla h \cdot \nabla v + \Pi(h) v \, d\mathbf{x}, \quad (8b)$$

where again we used integration by parts and $\mathbf{n} \cdot \nabla h = 0$ on the boundary $\partial \bar{\Omega}$. In particular this statement of the PDE implies conservation of volume

$$\frac{d}{dt} \int_{\bar{\Omega}} h(t, \mathbf{x}) \, d\mathbf{x} = 0,$$

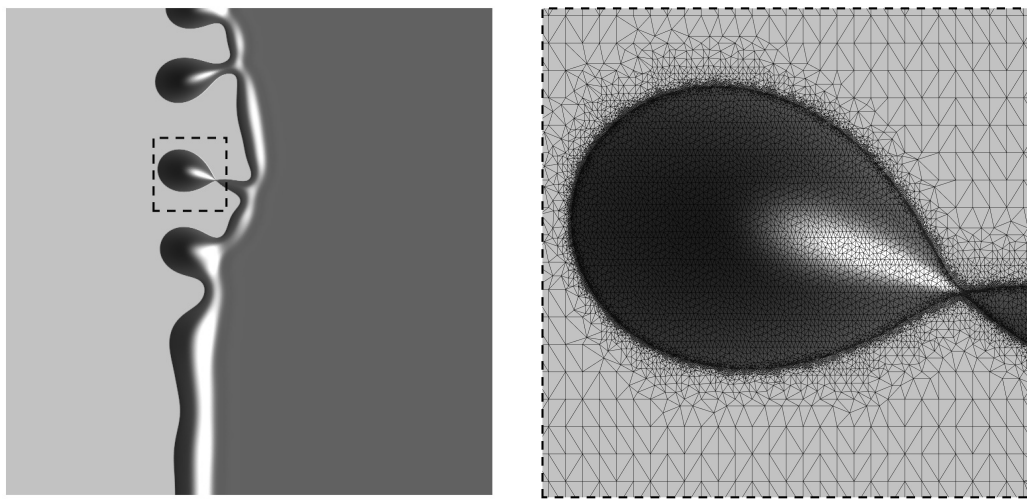


Fig. 5 (left) Dewetting rim during pinch-off of a single droplet highlighted with dashed lines and (right) magnification of this droplet and corresponding locally refined triangulation. The mesh consists of 92272 vertices, which requires to solve for $2 \times 368423 = 736846$ unknowns (h_n, π) for the P_2 FEM discretization at each time-step.

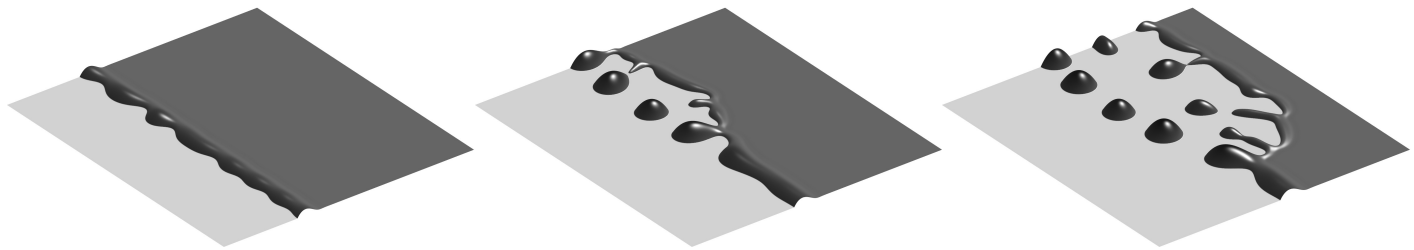


Fig. 6 Simulated pattern formation: 3D view with light shaded areas showing dry regions, whereas elevated darker areas indicate the liquid/air interface.

which can be seen when selecting $v = 1$ in the continuous or the discrete weak formulation. Evaluating the solution at discrete times $h_n(\mathbf{x}) = h(n\tau, \mathbf{x})$ we use the time-discretization $\partial_t h = \tau^{-1}(h_n - h_{n-1})$. This allows us to rewrite the weak form of the thin-film model in (8) so that we seek $(h_n, \pi) \in W$ such that

$$\int_{\bar{\Omega}} h_n v + \tau m^* \nabla \pi \cdot \nabla v \, d\mathbf{x} = \int_{\bar{\Omega}} h_{n-1} v \, d\mathbf{x}, \quad (9a)$$

$$\int_{\bar{\Omega}} \pi w - \nabla h_n \cdot \nabla w \, d\mathbf{x} = \int_{\bar{\Omega}} \Pi^* w \, d\mathbf{x}, \quad (9b)$$

which needs to hold for all (v, w) from a suitable function space W . When we define $m^* = m(h_{n-1})$ and $\Pi^* = \Pi(h_{n-1})$ this becomes a semi-implicit time-discretization. The FEM constitutes a method for the construction of a finite-dimensional subspace $W_h \subset W$, where we have an admissible decomposition $\bar{\Omega} = \bigcup_{k=1}^N \mathcal{T}_k$ of the domain into triangles \mathcal{T}_k , on which we define W_h as the space of continuous functions which are piecewise quadratic on each triangle, *i.e.* P_2 finite elements. Then we seek a discrete solution $(h_n, \pi) \in W_h$ of (9) valid for all $(v, w) \in W_h$. The integrals appearing in (9) are solved exactly or using 7-point Gauss quadrature. A typical droplet pattern emerging from the simulation with $m = h^2$ is shown in Fig. 6.

The main difficulties in solving (9) are due to the fact that one needs to choose the h_* contained in $\Pi(h)$ quite small. Then the solution h will feature large regions where the solution is either almost constant $h \approx h_*$ or the solution is smooth and $h \gg h_*$, as

shown in Fig. 2. However, where those regions meet the solution features a kink which should be resolved in the triangulation, cf. Fig. 5. We perform a heuristic local mesh refinement in these connecting regions, where the contact line is situated. Assuming the solution does not change drastically in time and having a finer mesh also in the neighborhood of this kink allows us to keep a locally refined mesh a number of discrete time-steps. When constructing a new mesh, we start from a coarse base mesh and determine which of its elements are crossed by the contact line

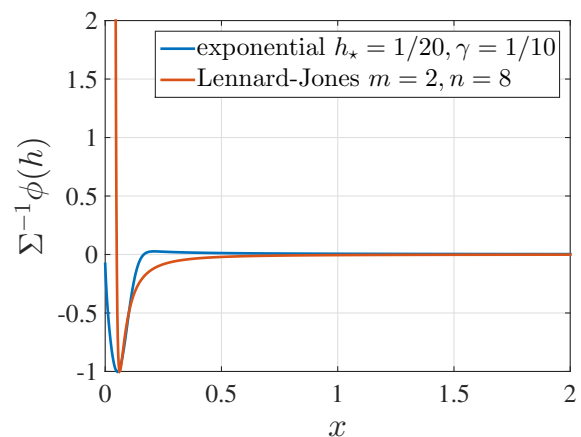


Fig. 7 Lennard-Jones potential (1) compared to the much more short-ranged exponential potential (10) both with $h_* = 1/20$, $\epsilon_* = 1/16$.

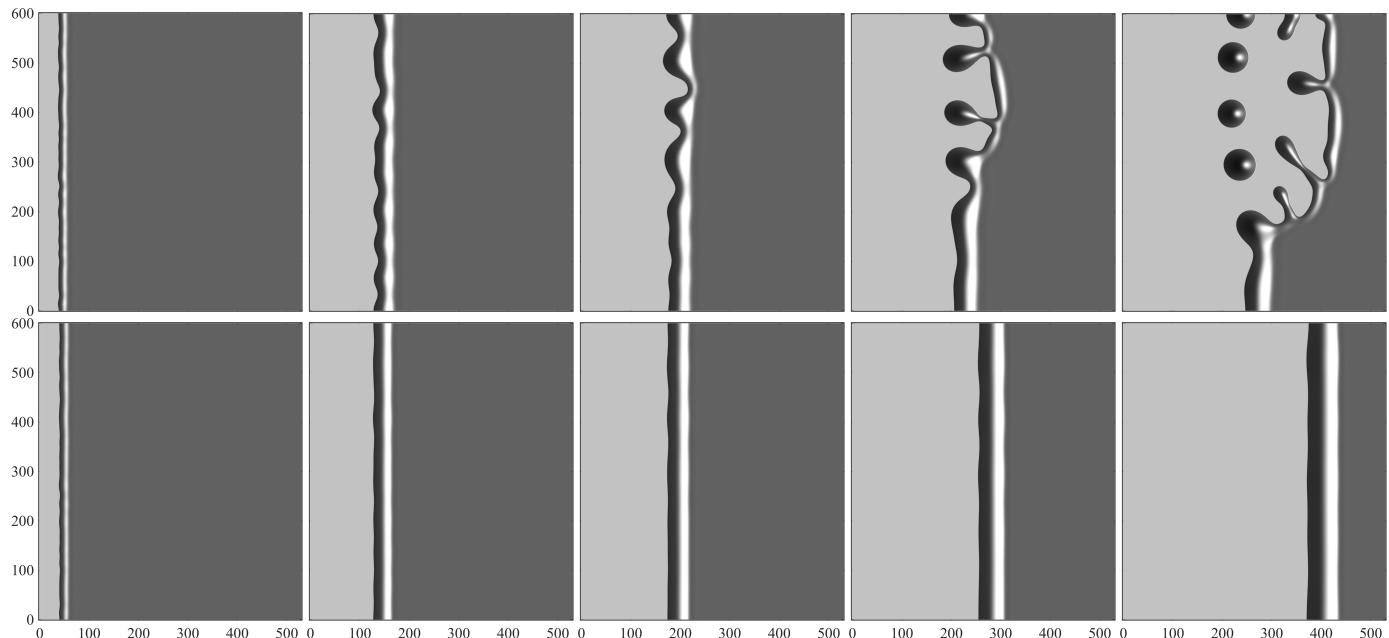


Fig. 8 Numerical solutions for (**upper**) mobility $m = h^2$ and (**lower**) mobility $m = h^3$ with initially straight front with random oscillating perturbation and time progressing from left to right (shown for similar rim progression)

of the previous solution. Those elements are refined by inserting additional vertices to an extend, that the kink is resolved again. Furthermore we make sure that also neighboring elements are refined. Based on the set of newly created vertices we perform a new triangulation and interpolate the old solution onto the new triangulation.

In order to allow the control of the minimum and the derivatives of ϕ separately via h_* and ε_* it is advantageous to work with an alternative potential representation $\phi(h) = \widehat{\phi}((h - h_*)/\varepsilon_*)$ with

$$\widehat{\phi}(s) = -\Sigma \left(\frac{\gamma}{1+s} - (1+\gamma) \exp(-s^2) \right), \quad (10)$$

which has similar properties as (1). In particular, with this potential we still have the same Γ -convergence property as $h_*, \varepsilon_* \rightarrow 0$. This abstract statement ensures that equilibrium contact angles are maintained and that the energetic contribution of ϕ from (10) and from (1) coincide in this limit. We note that for $0 < \gamma \ll 1$ the minimum slightly shifts away from h_* , however, one gains a slightly stabilizing potential with $\phi'' > 0$ for $h \gg h_*$. In addition we point out that we monitor that the minimum of the solution $\min_{\mathbf{x}} h(t, \mathbf{x})$ never violates the nonnegativity requirement that $\phi \rightarrow \infty$ as $h \rightarrow 0$ (see Fig. 7), in particular, by keeping the time-step size τ sufficiently small, see also previous mathematical studies^{46,47} that incorporate the nonnegativity property into their numerical scheme.

3.2 Initial data for rims and ridges

We still need to specify the initial data $h_0(\mathbf{x})$ for the numerical simulation in order to describe the various stages of the dewetting process. In experiments, the dewetting is started from a uniform flat layer bounded by a nearly straight edge. When the sample is heated the layer liquidifies and the edge becomes a moving

contact line of the dewetting process. In simulations we choose the supporting domain sufficiently large $\bar{\Omega} = [0, L] \times [0, 600]$ with $L \sim 500$, and using $h_* = 1/20$ we represent the uniform layer with the nearly straight contact line at x_0 using an initial film thickness

$$h_0(\mathbf{x}) = h_* + \frac{1}{2} \left(1 + \tanh \left[\frac{x - x_0(y)}{\delta} \right] \right), \quad (11)$$

with the smooth initial contact line position $x_0(y) = 20 + \sum_{n=1}^{50} a_n \cos(n\pi y/600)$. With $\delta = 1/2$ one can interpret h_0 to be an approximation of a step-like profile, where slight corrugations of x_0 along y -direction are introduced using the normally-distributed coefficients a_n with zero mean and standard deviation $1/10$. This choice is then maintained throughout all dewetting simulations for various mobilities.

For long times and domain size far beyond $\bar{\Omega}$, one can observe multiple dewetting rims colliding and forming capillary ridges. In order to study the stability of a capillary ridge, we first compute a 1D stationary solution $h_{\text{stat}}(x)$ and the linear stability with respect to perturbations $h(t, \mathbf{x}) = h_{\text{stat}}(x) + \delta h_1(x; k) e^{iky + \sigma t}$, with fixed wavenumber k , which returns an eigenproblem for the perturbation h_1 of the base state^{21,42}. Then we select an unstable mode k , usually the most unstable, and use initial data of the form

$$h_0(\mathbf{x}) = h_{\text{s}}(x) + \delta h_1(x; k) \cos(ky), \quad (12)$$

with a sufficiently small δ , so that also the non-negativity of h_0 is not violated. In the linear regime we expect to see an exponential amplification of the perturbation as indicated above, however, we are interested in using the numerical simulation as a tool to observe features in the nonlinear regime which are distinctive features of the ridge shape, *e.g.*, secondary or tertiary droplets, the general form of the intermolecular potential is the same but we

use $h_* = 1/40$. In order to study the systematic effect of the slip boundary condition on dewetting patterns, we study the contact-line instability of moving rims and stationary ridges for the mobility function $m(h) = h^3$ (no-slip) and $m(h) = h^2$ (intermediate-slip). In figure 8 the evolution of the rims for no-slip and intermediate-slip is shown at times, where they have accumulated the same volume, starting with the same initial film thickness as given in the experiments. This corresponds to the experimental results where the evolution of the rims are shown at the same distance measured from the initial coordinates. For the first time the striking dewetting patterns for the intermediate-slip case is observed, while for the no-slip case only shallow oscillation will accrue, in excellent comparison with the experimental results in Fig. 3

4 Break-up of a liquid ridge

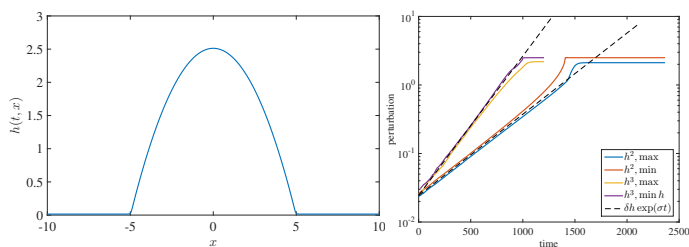


Fig. 9 (left) 1D steady state h_0 with $\epsilon_* = 1/20$, $h_* = 1/80$ and **(right)** amplification of a perturbation (13) to the initial state showing $\min_y h(t, x = 0, y)$ and $\max_y h(t, x = 0, y)$ from numerical solution with σ compared to the prediction of linear stability²¹ $h - h_0 \sim \exp(\sigma t)$ for h^2 and h^3 mobility.

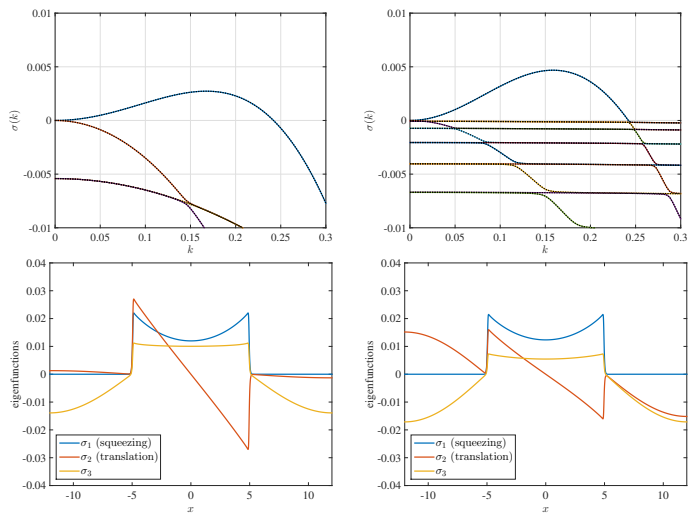


Fig. 10 Dispersion relation $\sigma(k)$ for **(upper left)** h^2 and **(upper right)** h^3 with overlapping results for exponential and standard potential (full and dotted lines), and below **(bottom)** the corresponding eigenmodes for most unstable wavenumber are shown.

Towards the final stages of dewetting process the rims approach each other and merge, yielding a polygonal network of ridges. As is known from previous studies stationary ridges are susceptible to Rayleigh-Plateau type instability for both no-slip and intermediate boundary conditions at the substrate. Both, the no-slip and the intermediate-slip case have been extensively investigated

in the literature^{21,24,26}.

4.1 Comparisons with linear stability analysis

We first summarise the linear stability of a (stationary) ridge, which is carried out by King et al.²¹ in detail. Stationary ridges appear as time-independent two-dimensional solutions of (3), that is, with $\partial_t h \equiv 0$, $\partial_y h \equiv 0$, with a constant film thickness $h \rightarrow h_c$ at $x \rightarrow \pm\infty$. An example for such a solution is shown on the left in Fig. 9, with a symmetric and approximately parabolic shape around the maximum. The defining boundary value problem invariant against translations and simultaneous rescaling of x and h , and therefore the solutions form a two parameter family, where each member is uniquely specified by the location and height of the maximum. A linear stability analysis that introduces perturbations of the form

$$h(t, x, y) = h_0 + \delta h_1(x; k) \exp(iky + \sigma t) \quad (13)$$

was carried out for (3) using asymptotic techniques. We summarise here only the salient features relevant to the comparison and discussion here.

Solving the eigenvalue problem for $\sigma(k)$ that results from introducing (13) numerically reveals that as $k \rightarrow 0$, the top two eigenvalues (i.e. with the largest real part) are real and tend to zero. The larger one is associated with the scale invariance and hence corresponds to varicose perturbations of the ridge and is the only eigenvalue that is positive, hence unstable for a range of wavenumbers $0 < k < k_c$ but stable for $k > k_c$.

The other mode results from the translation invariance and induces zig-zag perturbations; it is always stable. Further modes exist but they are all strictly negative for all k . Dispersion relations for several of the eigenvalues and the associated eigenfunctions h_1 are shown in the top and bottom row of Fig. 10. The results in the left and right columns are for different mobilities, that is, h^2 and h^3 .

An asymptotic analysis for the sharp interface limit $\epsilon \rightarrow 0$ reveals that to leading order²¹, the dispersion relation of the top eigenvalue only depends on the minimum value of $\phi(h_*)$ (and hence on the effective contact angle) but not on other details of the potential. To illustrate this point, we include also the dispersion relation using standard the potential (1), see dotted and full lines in Fig. 10.

4.2 Beyond linear theory

We now consider nonlinear simulations using the stationary ridge with very small monochromatic perturbations as initial data. Specifically, we consider four choices for k which satisfy

$$k < k_m, \quad k \approx k_m, \quad k_m < k < k_c, \quad k \approx k_c,$$

and carry out simulations with the mobilities h^2 , h^3 . The results are shown on the right of Fig. 9.

As long as the perturbations are small enough, the evolution of the corrugations in the nonlinear model closely follow the predictions from the linear stability analysis. Once the perturbations become comparable to the size of the rim ($\max_x |h - h_0| \approx 1$ for a

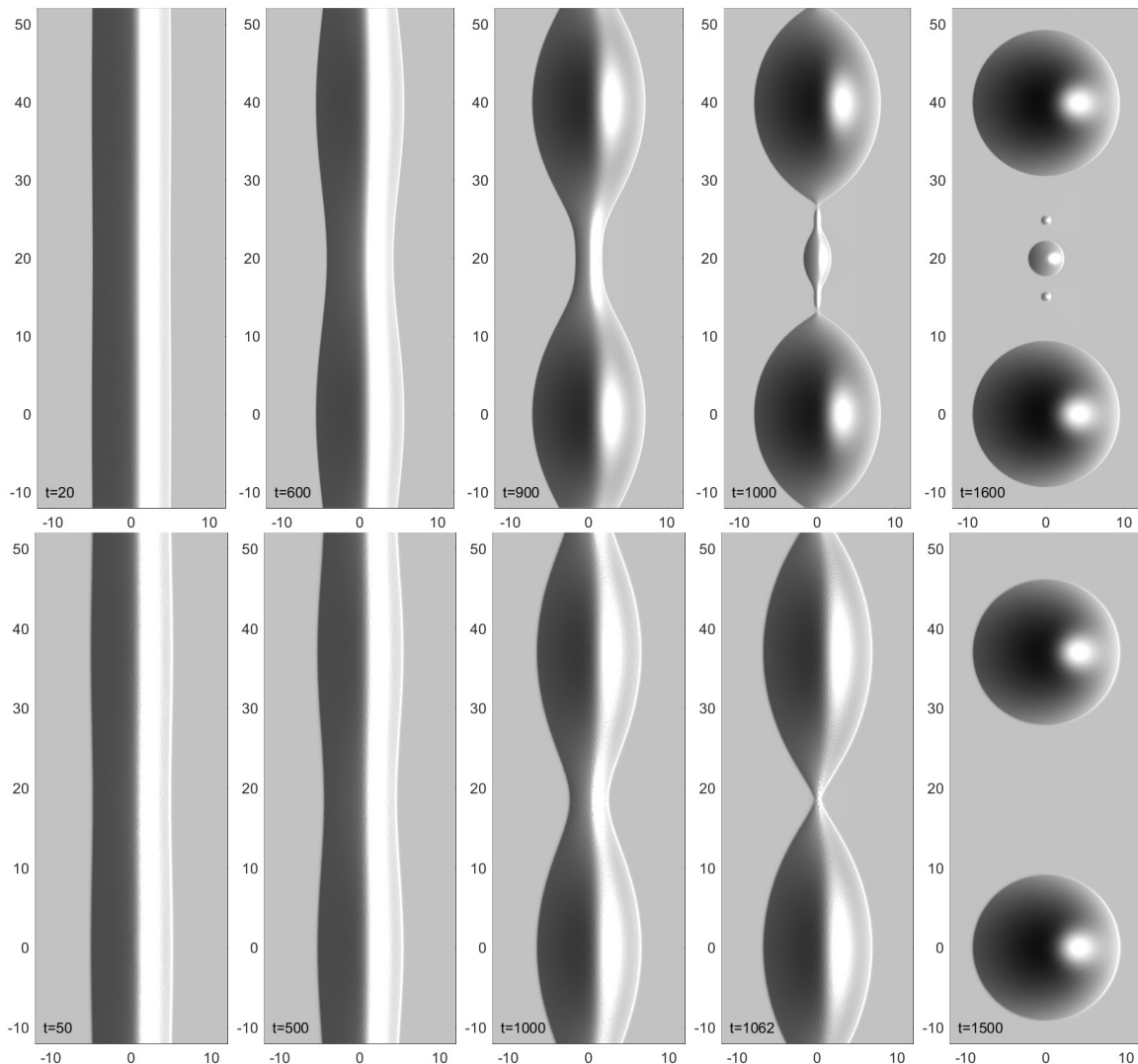


Fig. 11 Solution of thin-film problem with (top) $m(h) = h^3$ and (bottom) $m(h) = h^2$ and initial data $h(0, x, y) = h_0(x) + \delta h_1(k; x) \cos(ky)$ at different times. The wavenumber k is the one with the largest amplification σ from Fig. 10 and the domain $\Omega = [-12, 0] \times [0, \pi/k]$ is then extended to $[-12, 12] \times [-\pi/k, 3\pi/k]$ using the implied symmetry of the solution

base state with $\max_x h_0 = 2.5$), nonlinear terms become relevant and the growth rate changes.

Regarding the morphological evolution of the ridges for the no-slip and intermediate-slip case, our numerical simulations show qualitative and quantitative very similar behaviour during the linear regime. However, deep into the nonlinear regime the break-up into droplets follows different scenarios. In the no-slip case a cascade of satellite droplets emerge, while for the intermediate-slip case they disappear. Starting with the same initial condition, the evolution for both cases is shown in Fig. 11. Interestingly, this different behaviour is also observed in our experimental results as seen in Fig. 12.

5 Conclusion and discussion

We have introduced a highly adaptive FEM based numerical approach that correctly captures the complex dewetting process described by a class of thin-film models with degenerate mobilities. We showed that for the no-slip condition the droplet

pinch-off is absent during the retraction of the rim, while for the intermediate-slip case self-repeating droplet pinch-off occurs in excellent agreement with experimental results.

The ability to resolve the different length scales for long time scales enables also the prediction of new phenomena, such as the formation of satellite droplets as a function of the mobility. The emergence of satellite droplets is well-known during the break-up of liquid jets and the related problem of liquid filaments. For the latter problem destabilisation is due to the difference in the axial contribution to the capillary pressure between thicker and thinner parts. In this system the pressure is higher in the thinner parts and squeezes the liquid into the bulges, thus increasing the perturbation until the filament breaks up. Apart from the huge literature on experimental studies, the problem has sparked numerous numerical and analytical investigations^{28,48,49}. In particular the work by Tjahjadi et al.²⁷, where the emergence of satellite droplets was captured numerically, and highly the accurate numerical schemes developed by Kim et al.⁵⁰ improved the un-

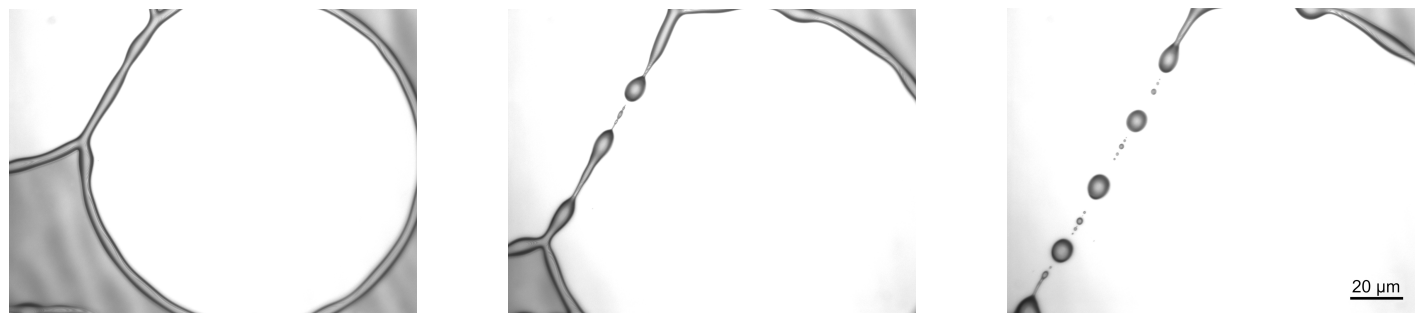


Fig. 12 Experimental results: Close-up of late stage dewetting of a rim of PS(10.3k) on AF 1600 with time progressing from left to right showing decay into satellite and subsatellite droplets. (Images: Courtesy of L. Marquant¹)

derstanding the underlying physical processes considerably.

For the situation of a ridge sitting on a solid substrate, considered here, the additional influence of the substrate is present and also enters the linear stability analysis, in particular through the contact angle. It will be interesting to investigate analytically the rupture behaviour for this problem to help understand the influence of the boundary condition at the substrate. Similarly it remains an interesting open question how the dissipation near a moving contact line would affect the whole pattern formation process. Such a study would certainly require more sophisticated finite element techniques⁵¹.

Acknowledgements

We thank Kirstin Kochems for technical assistance. DP acknowledges the financial support of the Einstein Foundation Berlin within the framework of the research center MATHEON.

Notes and references

- 1 L. Marquant, *PhD thesis*, 2013.
- 2 E. B. Dussan V., *Annual Review of Fluid Mechanics*, 1979, **11**, 371–400.
- 3 P. G. de Gennes, *Reviews of Modern Physics*, 1985, **57**, 827–863.
- 4 F. Brochard-Wyart and P. de Gennes, *Langmuir*, 1992, **8**, 3033–3037.
- 5 F. Brochard-Wyart and P. de Gennes, *C. R. Acad. Sci. Ser. II*, 1993, **327**, 13–17.
- 6 F. Brochard-Wyart, P.-G. de Gennes, H. Hervet and C. Redon, *Langmuir*, 1994, **10**, 1566–1572.
- 7 K. B. Migler, H. Hervet and L. Léger, *Phys. Rev. Lett.*, 1993, **70**, 287–290.
- 8 L. Léger, *J. Phys.: Condensed Matter*, 2003, **15**, S19–S29.
- 9 E. Lauga, M.P.Brenner and H. Stone, *Handbook of Experimental Fluid Dynamics*, Springer, New York, 2007, pp. 1219–1240.
- 10 L. Bocquet and J. L. Barrat, *Soft Matter*, 2007, **3**, 685–693.
- 11 C. Redon, F. Brochard-Wyart and F. Rondelez, *Phys. Rev. Lett.*, 1991, **66**, 715–718.
- 12 C. Redon, J. B. Brzoska and F. Brochard-Wyart, *Macromolecules*, 1994, **27**, 468–471.
- 13 G. Reiter and R. Khanna, *Langmuir*, 2000, **16**, 6351–6357.
- 14 K. Jacobs, R. Seemann, G. Schatz and S. Herminghaus, *Langmuir*, 1998, **14**, 4961–4963.
- 15 P. Damman, N. Baudelet and G. Reiter, *Phys. Rev. Lett.*, 2003, **91**, 216101.
- 16 R. Fetzer and K. Jacobs, *Langmuir*, 2007, **23**, 11617–11622.
- 17 J.-L. Masson, O. Olufokunbi and P. F. Green, *Macromolecules*, 2002, **35**, 6992–6996.
- 18 F. Brochard-Wyart and C. Redon, *Langmuir*, 1992, **8**, 2324–2329.
- 19 G. Reiter and A. Sharma, *Phys. Rev. Lett.*, 2001, **80**, 166103.
- 20 S. Haefner, M. Benzaquen, O. Bäumchen, T. Salez, R. Peters, J. D. McGraw, K. Jacobs, E. Raphaël and K. Dalnoki-Veress, *Nature communications*, 2015, **6**, 7409.
- 21 J. King, A. Münch and B. Wagner, *Nonlinearity*, 2006, **19**, 2813–2831.
- 22 A. Münch, B. Wagner and T. P. Witelski, *J. Engr. Math.*, 2006, **53**, 359–383.
- 23 K. Kargupta, A. Sharma and R. Khanna, *Langmuir*, 2004, **20**, 244–253.
- 24 S. H. Davis, *Journal of Fluid Mechanics*, 1980, **98**, 225–242.
- 25 K. Sekimoto, R. Oguma and K. Kawasaki, *Annals of Physics*, 1987, **176**, 359–392.
- 26 J. A. Diez, A. G. González and L. Kondic, *Physics of Fluids*, 2009, **21**, 082105.
- 27 M. Tjahjadi, H. A. Stone and J. M. Ottino, *Journal of Fluid Mechanics*, 1992, **243**, 297–317.
- 28 J. Eggers and E. Villermaux, *Reports on Progress in Physics*, 2008, **71**, 036601.
- 29 R. Seemann, S. Herminghaus and K. Jacobs, *Physical Review Letters*, 2001, **86**, 5534.
- 30 R. Seemann, S. Herminghaus and K. Jacobs, *Journal of Physics: Condensed Matter*, 2001, **13**, 4925.
- 31 O. Bäumchen, L. Marquant, R. Blossey, A. Münch, B. Wagner and K. Jacobs, *Phys. Rev. Lett.*, 2014, **113**, 014501.
- 32 P. L. Evans, J. R. King and A. Münch, *Applied Mathematics Research eXpress*, 2006, **2006**, 1–25.
- 33 R. Fetzer, K. Jacobs, A. Münch, B. Wagner and T. P. Witelski, *Phys. Rev. Lett.*, 2005, **95**, 127801.
- 34 R. Fetzer, A. Münch, B. Wagner, M. Rauscher and K. Jacobs, *Langmuir*, 2007, **23**, 10559–10566.

- 35 R. Fetzer, M. Rauscher, A. Münch, B. A. Wagner and K. Jacobs, *Europhysics Letters (EPL)*, 2006, **75**, 638–644.
- 36 O. Bäumchen, R. Fetzer and K. Jacobs, *Phys. Rev. Lett.*, 2009, **103**, 247801.
- 37 O. Bäumchen and K. Jacobs, *J. Phys. Condens. Matter*, 2010, **22**, 033102.
- 38 J. C. Flitton and J. R. King, *J. Engr. Math.*, 2005, **50**, 241–266.
- 39 J. D. McGraw, O. Bäumchen, M. Klos, S. Haefner, M. Lessel, S. Backes and K. Jacobs, *Advances in colloid and interface science*, 2014, **210**, 13–20.
- 40 A. Münch and B. Wagner, *Physica D*, 2005, **209**, 178–190.
- 41 M. Dziwnik, M. Korzec, A. Münch and B. Wagner, *Multiscale Modeling & Simulation*, 2014, **12**, 755–780.
- 42 J. King, A. Münch and B. Wagner, *J. Engrg. Math.*, 2009, **63**, 177–195.
- 43 O. Lessel, O. Bäumchen, M. Klos, H. Hähl, R. Fetzer, M. Paulus, R. Seemann, and K. Jacobs, *Surf Interface Anal.*, 2015, **47**, 557.
- 44 O. Bäumchen, R. Fetzer, M. Klos, O. Lessel, L. Marquant, H. Hähl and K. Jacobs, *J. Phys.:Condens. Matter*, 2012, **24**, 325102.
- 45 O. Bäumchen, R. Fetzer, A. Münch, B. Wagner and K. Jacobs, *IUTAM Symposium on advances in micro- and nanofluidics*, 2009, 0 ISBN: ISBN 2–906831–76–X.
- 46 L. Zhornitskaya and A. L. Bertozzi, *SIAM Journal on Numerical Analysis*, 1999, **37**, 523–555.
- 47 G. Grün and M. Rumpf, *Numerische Mathematik*, 2000, **87**, 113–152.
- 48 J. Eggers, *Rev. Mod. Phys.*, 1997, **69**, 865–930.
- 49 A. L. Bertozzi, *ZAMM - Journal of Applied Mathematics and Mechanics / Zeitschrift für Angewandte Mathematik und Mechanik*, 1996, **76**, 373–419.
- 50 J. Kim, K. Kang and J. Lowengrub, *Journal of Computational Physics*, 2004, **193**, 511 – 543.
- 51 D. Peschka, *Physics of Fluids*, 2018, **30**, 082115.